Combining UAV and Landsat data to assess glacier changes on the central Tibetan Plateau

Yuang Xue[1,2] , Zhefan Jing[1], Shichang Kang[1,2,3], Xiaobo He[1,4] and Chenyu Li[1,2]

[1]State Key Laboratory of Cryospheric Science, Northwest Institute of Eco-environment and Resources, Chinese Academy of Sciences (CAS), Lanzhou 730000, China; [2]University of Chinese Academy of Sciences, Beijing 100049, China; [3]CAS Center for Excellence in Tibetan Plateau Earth Sciences, Beijing 10010, China and [4]Tanggula Cryosphere and Environment Observation Station, State Key Laboratory of Cryospheric Sciences, Lanzhou 730000, China

Abstract

In recent years, researchers have focused on the applications of uncrewed aerial vehicles (UAVs) in environmental remote sensing tasks. However, studies on glacier monitoring using UAV technology are relatively scarce, especially for high mountain glacier monitoring. To explore the feasibility of UAV technology for high mountain glaciers, four UAV surveys were deployed on two glaciers of the central Tibetan Plateau. Based on the images retrieved by UAV in 2017 and 2019, orthomosaics and digital elevation models were produced to quantify the length, area and elevation changes in the ablation zone of these two glaciers at different times. Additionally, we utilized several Landsat scenes to derive glacier changes over the last 30 years and combined these with the UAV data to assess the advantages and disadvantages of UAV technology in mountain glacier monitoring.

1. Introduction

The Tibetan Plateau (TP), which is one of the regions with the highest glacier concentration outside the polar region, is the source region of all the large rivers in Asia (Immerzeel and others, 2010; Yao and others, 2012; Zhang and others, 2018). Impacted by climate warming, most of the glaciers on the TP have undergone great mass loss over the past 30 years, which may lead to unsustainable water supplies for major rivers and threaten the livelihoods of people in the downstream regions (Kang and others, 2010; Yao and others, 2012; Liang and others, 2019). The best way to understand how climate perturbations impact the status of glaciers is to monitor glacier changes (Immerzeel and others, 2014; Paul and others, 2015). However, the field observations of TP glaciers remain scarce due to inaccessibility, the harsh climate and the high cost (Rossini and others, 2018; Zhang and others, 2018).

Satellite remote sensing measurements of glacier changes complement field observations. In particular, Landsat imagery with long time series archives has been proven an efficient tool for mapping glacier areas and monitoring glacier changes, even for small glaciers (Kääb and others, 2002; Paul and others, 2002; Andreassen and others, 2008; Fischer and others, 2015). Existing methods using multispectral images to outline boundaries for debris-free glaciers are mature (Paul and others, 2015). However, most satellite data still present some fundamental challenges for glacier monitoring, such as low spatiotemporal resolution and high cost (Whitehead and others, 2013). Additionally, cloud cover is a notable issue in the mountain regions (Wigmore and Mark, 2017).

Uncrewed aerial vehicles (UAVs) have a history in military applications (Vallet and others, 2011). In the last two decades, this technology has been applied in the civil domain and has created a new remote sensing market (Colomina and Molina, 2014). UAV technology can make up for the shortcomings of satellite remote sensing and traditional surveys. It is now possible to acquire both high-resolution orthomosaics and topography of targets using photogrammetric software and a consumer-grade camera that is mounted on a lightweight UAV. Currently, the use of UAVs in the field of earth science is undergoing rapid expansion because of the ultra-high spatiotemporal resolution and low-cost benefits of UAV technology (Kraaijenbrink and others, 2016b; Wigmore and Mark, 2017; Zmarz and others, 2018; Carrera-Hernández and others, 2020; Giordan and others, 2020). Nevertheless, UAV-based glaciology research is a very small part of all UAV-based environmental research.

In glaciology, the first published paper of UAV applications focused on the polar region (Hodson and others, 2007), and such interest has continued to grow. Subsequently, UAV technology has been successfully applied in research on Himalayan and Alpine glaciers. For example, Immerzeel and others (2014) performed three UAV surveys on a debris-covered Himalayan glacier for the first time and indicated that UAV technology may revolutionize classical field-based methods; Benoit and others (2019) conducted ten UAV surveys on an Alpine glacier without GCPs; they extracted the coordinates of the bedrocks around the glacier from one survey product and used them to co-register the remaining products. However, the number of studies on UAV-based high mountain glaciers is low compared with the alpine and polar regions, especially for those mountain glaciers on the TP. To our knowledge, current research on UAV-based high mountain glaciers only involves five TP glaciers. They are Changeri Nup glacier (Vincent and others, 2016; Brun and others, 2018), Langtang glacier (Kraaijenbrink
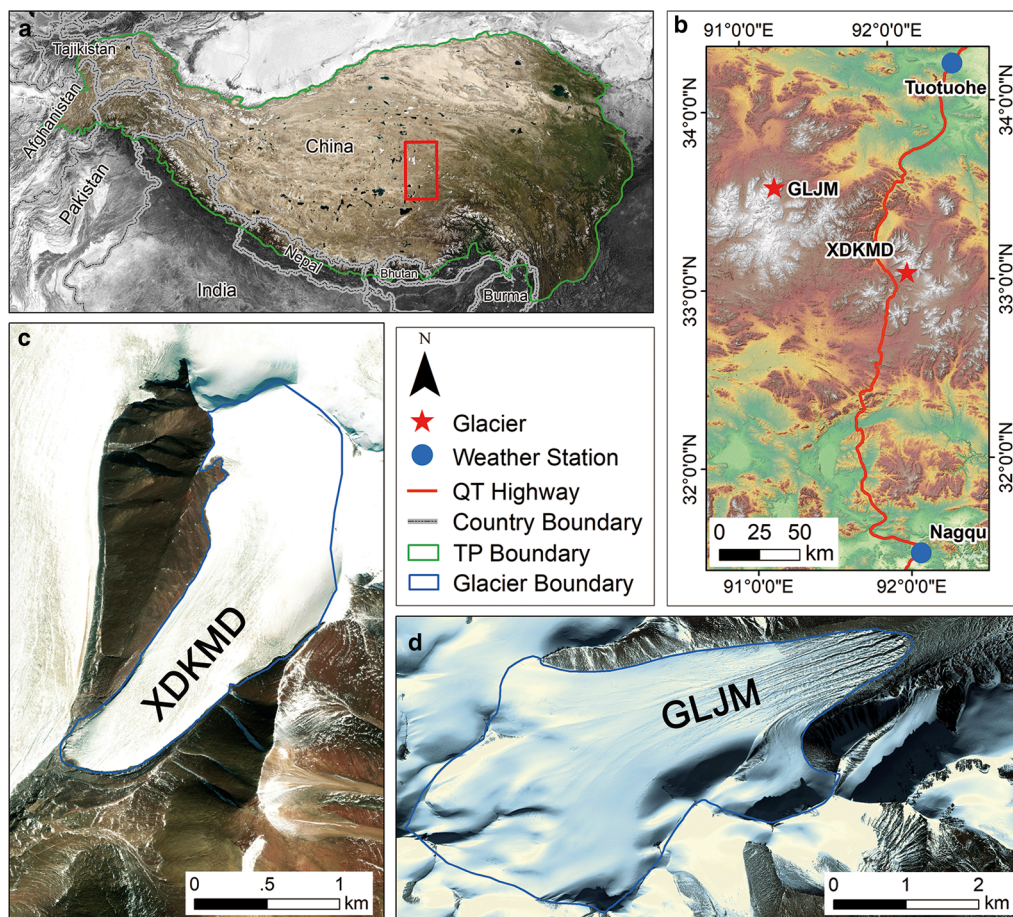
Fig. 1. Overview of the study area. (a) Extent of the TP; our study sites are on the central TP. (b) Details of our study sites. (c) Aerial view of XDKMD Glacier (source: Esri, Maxar). (d) Aerial view of GLJM Glacier (source: Bing Maps). Both glacier boundaries are obtained from CGI-2 (Guo and others, 2015).

Fig. 2. Photos of GLJM Glacier taken in July. (a) Erosional features in the terminus of GLJM Glacier. (b) The ice on the glacier terminal river.

and others, 2016*b*), Lirung glacier (Immerzeel and others, 2014; Brun and others, 2016; Buri and others, 2016; Kraaijenbrink and others, 2016*a*, 2018), Baishui River No. 1 glacier (Che and others, 2020) and Parlung No. 4 glacier (Yang and others, 2020). Moreover, these five glaciers are all distributed in the south and southeast TP. Little glacier research on the central TP has included UAV deployment.

In this paper, four high-resolution UAV surveys were conducted over Xiao Dongkemadi (XDKMD) Glacier and Ganglongjiama (GLJM) Glacier in 2017 and 2019 to obtain glacier changes in the short term. Additionally, we utilized several Landsat scenes to depict changes in the two glaciers over the last 30 years and chose a 10-year interval between two selected images due to the coarse spatial resolution. The main objectives of this study were (1) to apply a UAV for central TP glaciers and verify its feasibility and (2) to shed light on the long- and short-term changes in XDKMD Glacier and GLJM Glacier.

2. Study area

XDKMD Glacier (33°04′N, 92°04′E) and GLJM Glacier (33°34′N, 91°12′E) are located in the Tanggula Mountains of the central TP (Fig. 1). Both glaciers are typical continental glaciers in the Yangtze River source region (Zhang and others, 2018) and have a mean elevation that exceeds 5000 m above sea level (a.s.l.). The climate in this region is mainly influenced by the westerlies and monsoons. Thus, it presents cold, arid, windy winters and warm, wet summers (Liang and others, 2019), that is, precipitation mainly occurs in summer when the temperature is high. Therefore, the most dynamic season, when the accumulation and ablation processes of glaciers occur synchronously, is summer (i.e. from June to September, hereafter referred to as the ablation season).

XDKMD Glacier is a southwest-facing tributary glacier, with an area of 1.705 km^2; its terminal altitude changed from 5380 m in 1996 to 5420 m in 2013 (Zhang and others, 2013). XDKMD Glacier has been observed since 1989 (Pu and others, 2008), and an observation station was built in 2005 beside Qinghai-Tibet Highway. The travel time from the station to XDKMD Glacier is approximately two hours. The station now has relatively long-term records of mass balance of XDKMD Glacier, which are the second longest after Urumqi Glacier No. 1 in High Mountain Asia (Pu and others, 2008; Zhang and others, 2013).

GLJM Glacier is located in the northeast corner of Geladaindong, which is a nature reserve in the Yangtze River source region (Ye and others, 2006). According to the Second Chinese Glacier Inventory, the GLJM Glacier area in 2007 was 12.3 km^2, with a maximum altitude of 6106 m and a minimum altitude of 5224 m (Guo and others, 2015). The field observations of GLJM

Table 1. Utilized Landsat scenes

Glacier	Purpose	Path/row	Date	Sensor	Resolution (m)	Data type
XDKMD	Change	138/37	23/04/1988	TM	30	MTL
		138/37	09/08/1998	TM	30	MTL
		138/37	10/07/2008	TM	30	MTL
		138/37	17/04/2018	OLI	15	Pansharpened
	Comparison	138/37	27/09/2019	OLI	15	Pansharpened
GLJM	Change	138/37	05/09/1988	TM	30	MTL
		137/37	17/09/1998	TM	30	MTL
		138/37	12/09/2008	TM	30	MTL
		138/37	24/09/2018	OLI	15	Pansharpened
	Comparison	138/37	07/10/2017	OLI	15	Pansharpened
		138/37	27/09/2019	OLI	15	Pansharpened

In the seventh column, MTL means multispectral and Pansharpened means the fused image of panchromatic and multispectral images.

Table 2. Overview of the UAV campaigns performed in the ablation zone of the two study glaciers

Tag	Glacier	Date	Coverage (km²)	Flight altitude (m)	Resolution of orthomosaic/DEM (cm)	Number of photos taken (valid photos)
1	XDKMD	20/07/2019	0.548	150	3.24/12.9	449 (232)
2	XDKMD	27/09/2019	1.19	200	6.90/13.8	348 (334)
3	GLJM	06/07/2017	2.07	100	8.85/35.4	514 (354)
4	GLJM	16/10/2019	2.33	200	6.36/12.7	570 (558)

Glacier, which are challenging, started in 2017. As the travel time from the station to the GLJM Glacier is ~1 d, we need to camp there without a mobile signal for a few days to finish our fieldwork. The terminal surface of GLJM Glacier is very broken and forms some erosional features (Fig. 2a). Meltwater flows from the glacier and forms a river at the terminus. A thick layer of ice forms on this river and melts gradually during the ablation season (Fig. 2b).

3. Data and methodology

3.1 Landsat imagery

Currently, the publicly available remote sensing data commonly used for glacier delineation are Landsat and Sentinel-2. Landsat data have a longer time series; the resolution of visible, near-infrared (NIR) and short-wave infrared (SWIR) bands can be improved to 15 m after pan-sharpening (Landsat 7/8). Sentinel-2 data have a resolution of 10 m in visible and NIR bands, but a resolution of 20 m in SWIR band. Consider the method we used (NIR/SWIR), we could get higher resolution results with Landsat data. Therefore, we selected eight optimal Landsat scenes from 1988 to 2018 based on the cloud and snow cover conditions, with an image interval of 10 years. Additionally, another two scenes in 2017 and 2019 were selected for the comparison of the outlines from the UAV and Landsat (Table 1). All the scenes were provided by United States Geological Survey (USGS) (https://earthexplorer.usgs.gov) and orthorectified automatically by USGS using SRTM3 DEM (level 1 T). According to the research of Guo and others (2012), Landsat data have high precision, and most of them have correction accuracies of approximately half a pixel or more.

3.2 UAV surveys

In this study, a DJI Phantom 4 Pro quadcopter UAV was employed to conduct four surveys on the ablation zone of XDKMD Glacier and GLJM Glacier during the ablation season (refer to Table 2). The Phantom 4 Pro is equipped with a 20 MP digital compact camera with a built-in, three-axis stabilization system. With a 1.388 kg ultra-light body, the UAV is capable of ~30 min of flight at a speed of 50 kph in positioning mode

(DJI, 2017). However, the battery conversion rate will be greatly reduced in cold, low-pressure and high-altitude conditions, and the maximum tested photographing time with one battery is 15 min when the UAV takes off above 5000 m a.s.l.

The details of these surveys are shown in Figure 3. The UAV flew automatically along the flight course predefined by Pix4Dcapture (https://www.pix4d.com/product/pix4dcapture) and took photographs at a certain time interval. The position and attitude of the UAV at the exposure stations, which were obtained by the built-in integrated Position and Orientation System (POS, composed of global positioning system and inertial measurement units), were recorded in the JPEG pictures. However, we discovered that the altitude error of the final products exceeded 200 m without GCPs in the first survey of XDKMD Glacier, and thus, we set up four and three GCPs to improve the accuracy in the following surveys in September and October, respectively. The GCPs were composed of 1.5 by 1.5 m of red waterproof cloths with a yellow cross in the center distributed on the lateral moraine and glacier surface. The coordinates of the centers of the markers were measured using a Trimble GeoXT handheld GPS receiver, which can provide sub-meter accuracy with real-time or post-processed differential correction.

3.3 UAV data processing

UAV images in each survey were separately processed with Pix4Dmapper (Pix4D) in a three-step workflow, which is described below:

(1) *Initial processing*: This process generates a sparse point cloud with the structure-from motion algorithm (Turner and others, 2012). First, it searches for and matches key points in the photos that have certain overlapping areas using a feature matching algorithm (e.g. the scale-invariant feature transform (SIFT) algorithm, which can detect key points in photos with different views and illumination conditions; Lowe, 1999, 2004). Second, the approximate locations and orientations of the camera at each exposure station are reconstructed with the internal parameters (focal length, coordinates of the principal point of the photograph), and external parameters (i.e. POS data). A sparse point cloud is created.
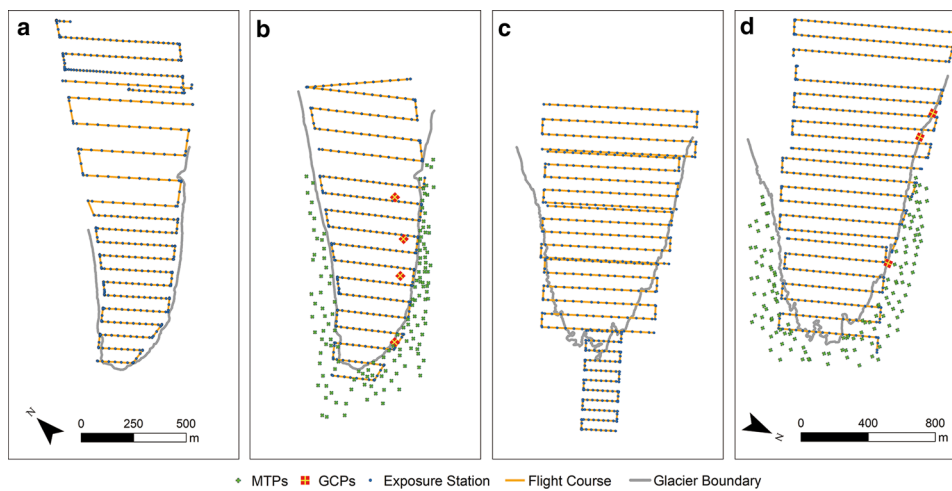
Fig. 3. Flight course of four UAV surveys: (a) 20/07/2019 in XDKMD Glacier, (b) 27/09/2019 in XDKMD Glacier, (c) 06/07/2017 in GLJM Glacier, (d) 16/10/2019 in GLJM Glacier.
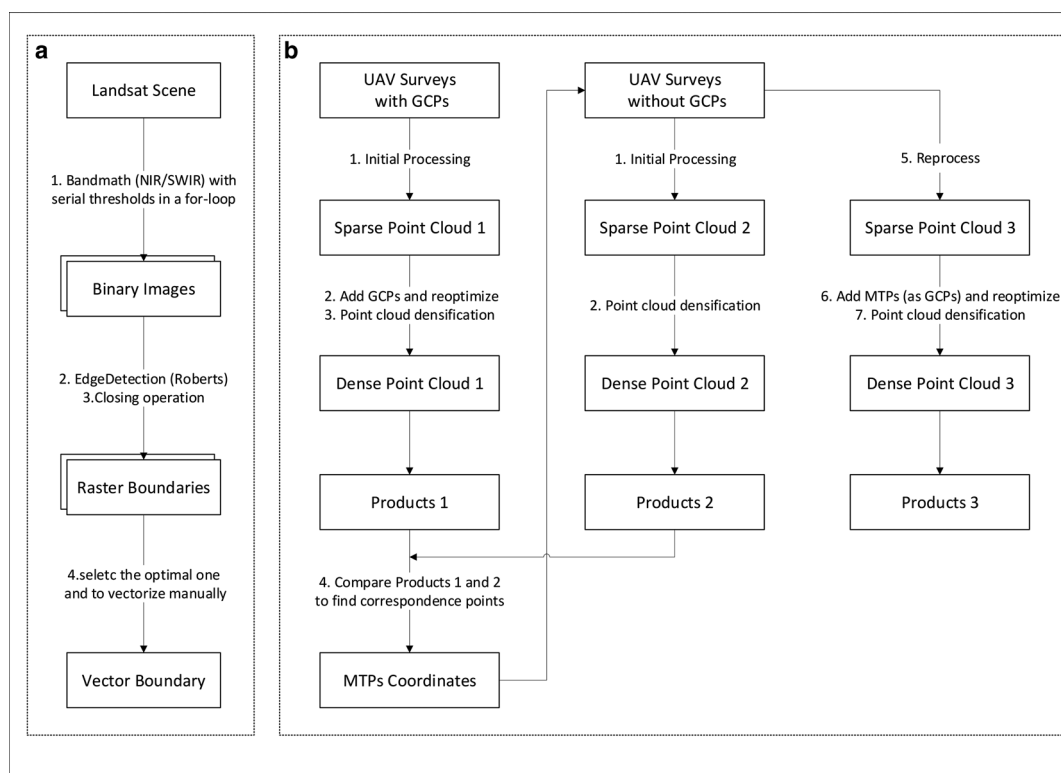
MTPs · GCPs · Exposure Station — Flight Course — Glacier Boundary

Fig. 4. Workflows of glacier delineation (a) and how we co-register the UAV data (b).

(2) *Point cloud densification*: In this step, the multi-view stereo technique is applied to achieve a higher point cloud density than in the previous step (Furukawa and Ponce, 2010; Mölg and Bolch, 2017). Thus, the spatial resolution of the products can be increased, and an irregular network for the next step can be created (Küng and others, 2012).

(3) *Digital elevation model (DEM) and orthomosaic generation*: DEM and orthomosaic are the two main final products. DEM can be built from dense point cloud or irregular network, and the former one usually has higher accuracy for rugged terrain. Every image pixel is projected on DEM and the georeferenced orthomosaic is generated (Küng and others, 2012).

During this process, we found photos with too much snow coverage that cannot be matched, that is, few feature points can be detected and matched in those photos, especially in survey 1, where almost half of the photos are invalid (Table 2). These issues also occur in the landscape with a homogeneous surface (e.g. still

water) as these surface features do not provide enough of the visible attributes needed for algorithms such as SIFT (Harwin and Lucieer, 2012).

We did not set GCPs in surveys 1 and 3, and the GCPs in surveys 2 and 4 were not well distributed. Thus, to accurately identify changes in the glaciers from the UAV images, the products of surveys 1 and 3 (Table 2, first column) need to be co-registered to the references of surveys 2 and 4 (Immerzeel and others, 2014; Benoit and others, 2019). Figure 4b illustrates the workflow of co-registration process. Consider the XDKMD Glacier, for example. First, we processed the data from surveys 1 and 2 to obtain the final products. We compared their orthomosaics to find some stable, well-marked surface features as manual tie points (MTPs). Second, we extracted the MTPs coordinates from the products of survey 1 and applied them as GCPs to reprocess the data from survey 2. Last, we obtained co-registered products of survey 2. Thus, the products at different times could be overlapped and the change of XDKMD Glacier could be detected.
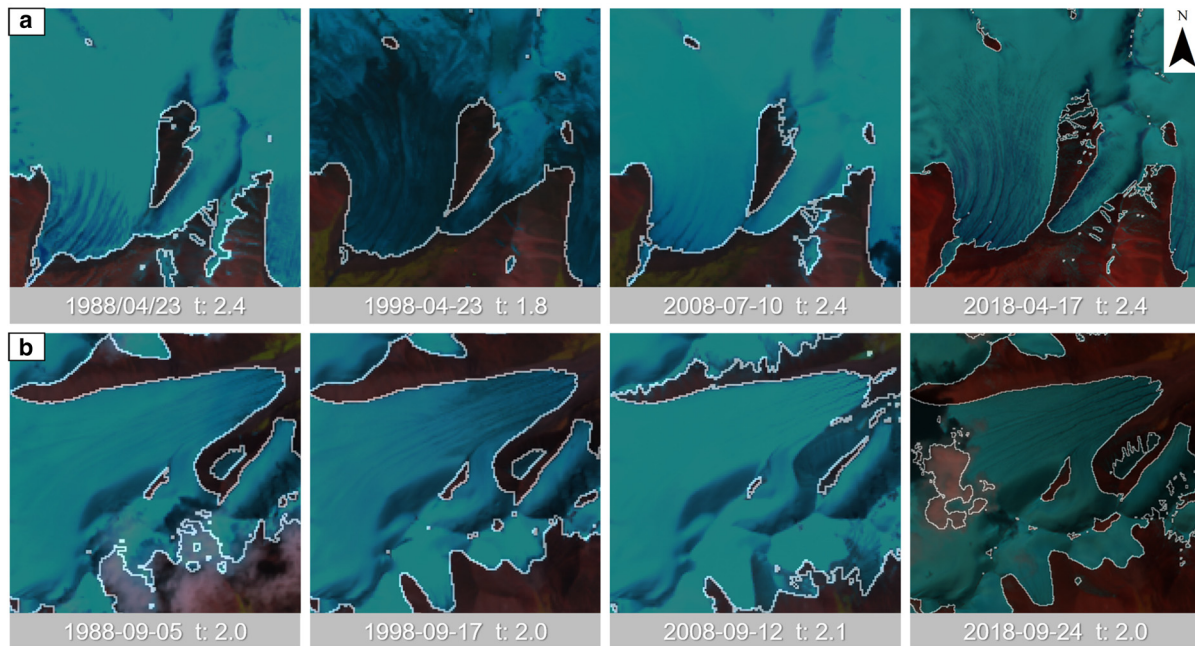
Fig. 5. Optimal threshold (*t*) that we selected for each Landsat scene of XDKMD Glacier (group A) and GLJM Glacier (group B).
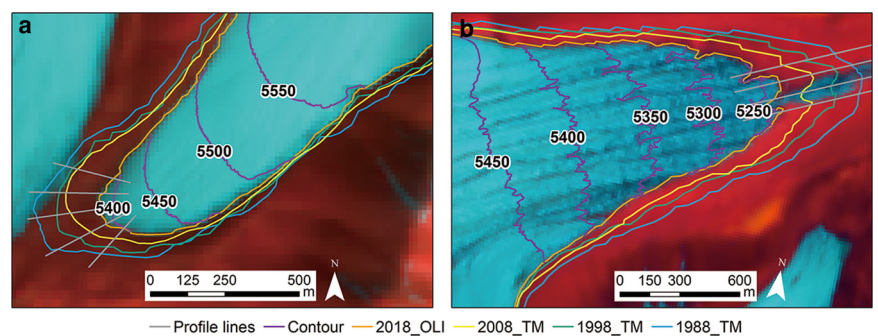

Fig. 6. Borders of the tongue of XDKMD Glacier (a) and GLJM Glacier (b) from 1988, 1998, 2008 and 2018 were outlined based on the Landsat TM/OLI data.

Table 3. Comparison of the outlines from UAV and Landsat

Glacier (region)	Landsat		UAV		
	Date	Area (km^2)	Date	Area (km^2)	Deviation (%)
XDKMD (<5550 m)	27/09/2019	0.2687	27/09/2019	0.2676	0.41
GLJM (<5450 m)	07/10/2017	1.0701	21/09/2017	1.0663	0.36
GLJM (<5450 m)	27/09/2019	1.0872	17/10/2019	1.0803	0.64

The MTPs utilized for the co-registration are mostly bedrocks and boulders with a width range of 1–3 m. To further confirm that the selected MTPs are stable, we need to check that the size, shape and surrounding features (e.g. stone, riverway) of these MTPs are the same between two repeated surveys. The geographic coordinates of the MTPs can be easily extracted in the pix4Dmapper. And in the end, we selected 143 MTPs and 136 MTPs from the products of survey 2 and survey 4, respectively.

3.4 Glacier delineation

3.4.1 Landsat

Previous studies have suggested that one of the most effective methods for glacier mapping is NIR/SWIR band ratio, which utilizes the large difference in spectral signature between snow and other materials in these spectral bands (Andreassen and others, 2008; Bolch and others, 2010). The whole process is implemented via automatic batch processing based on programming (Fig. 4a).

For one Landsat scene, first, a 'ratio image' is computed from the raw digital numbers for bands NIR/SWIR, and several different binary images are generated by setting a sequence of empirical thresholds (from 1.5 to 2.5, step size of 0.1; Fig. 5). Second, the raster boundaries with different thresholds are generated via edge detection (Roberts Operation) and denoised by the closing operation. Last, we select the best matching boundary for every scene to vectorize them manually. Thus, the change in the glacier margins is depicted in the overlay map using different polygons. Additionally, the method of drawing profile lines (Fig. 6) in different directions on the glacier terminus is adopted to compare the terminus changes and calculate the average rate of glacier retreat (Li and others, 1998; Cao and others, 2006).

3.4.2 UAV

The super-high resolutions of the UAV products make it easier and more accurate for us to manually outline the glacier
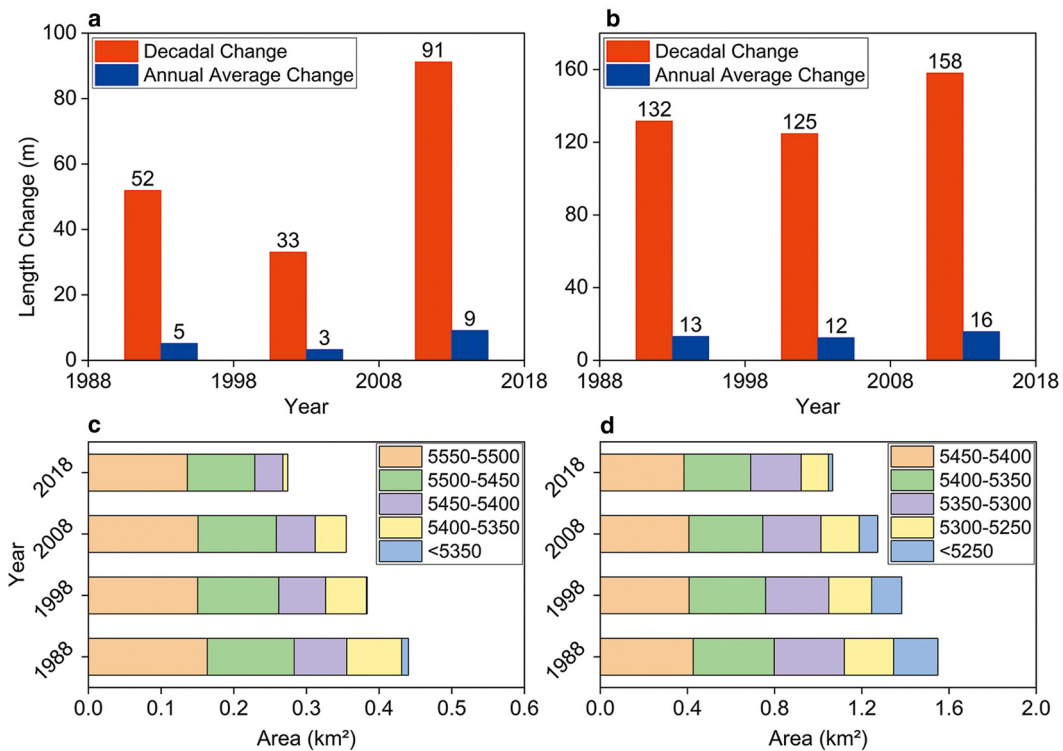
Fig. 7. Changes in the termini over the last 30 years. (a) and (b) show the changes in the lengths of XDKMD Glacier and GLJM Glacier, respectively; (c) and (d) show the changes in area of XDKMD Glacier and GLJM Glacier, respectively.

Table 4. XDKMD Glacier area change (AC) and area change rate (ACR) at different elevation intervals

Elevation (m)	23/04/1988–09/08/1998		09/08/1998–10/07/2008		10/07/2008–17/04/2018		23/04/1988–17/04/2018	
	AC (km² 10⁻²)	ACR (%)	AC (km² 10⁻²)	ACR (%)	AC (km² 10⁻²)	ACR (%)	AC (km² 10⁻²)	ACR (%)
5500–5550	−1.32	−8.1	0.05	0.3	−1.47	−9.8	−2.75	−16.8
5450–5500	−0.81	−6.8	−0.38	−3.4	−1.49	−13.9	−2.69	−22.4
5400–5450	−0.77	−10.7	−1.10	−17.0	−1.48	−27.7	−3.35	−46.4
5350–5400	−1.95	−25.7	−1.35	−24.0	−3.60	−84.4	−6.89	−91.2
<5350	−0.84	−88.2	−0.11	−100.0	0.00	Null	−0.95	−100.0
Total	−5.69	−12.9	−2.89	−7.5	−8.05	−22.7	−16.62	−37.7

boundaries. In most cases, we directly outlined the glacier boundary based on the orthomosaic. For some parts with snow cover, we employed the hillshade assist for recognizing the boundary. Similarly, we calculated the average length of several profile lines we drew at the terminus as the average retreat length of the glacier.

3.5 Error estimation

High-resolution UAV images were applied to quantify the accuracy of the glacier delineation from Landsat imagery. Our study area is clean and small without the need for further co-registration; so the main error is the uncertainty related to the glacier delineation. This uncertainty depends on the image resolution (Hall and others, 2003). Thus, we confirm the magnitude of this error based on the comparison of outlines from UAV and Landsat (Table 3).

We use the elevation change in the off-glacier area to assess the error of co-registration between repeated UAV surveys. The influence of glacier movement to its surrounding terrain exists but can be disregarded over a relatively short term. Thus, the elevation difference in the off-glacier area should be near zero. We have outlined several off-glacier zones and extracted their elevation difference to quantify the accuracy of the co-registration.

4. Results

4.1 Glacier changes over the last 30 years observed from Landsat imagery

The most direct evidence of the shrinkage of the two glaciers is the change in their termini. The terminus of XDKMD Glacier was connected to its main glacier at one time, but it was found to have separated from the main glacier during the field observation at the end of 2007 (Qiao, 2010). Moreover, the GLJM Glacier surface became broken due to the formation of supra-glacial drainage (which is shown in Section 4.2). We outlined the boundaries of XDKMD Glacier and GLJM Glacier based on the Landsat imagery and discovered that both glaciers retreated rapidly over the past 30 years. The glacier terminus decreased 176 m from 1988 to 2018 at a rate of 5.9 m a⁻¹, and the change rate in the third decade (third bar in Fig. 7a) was the fastest, which was also observed with GLJM Glacier. However, it seems that GLJM Glacier retreated more dramatically; the comparison of the outlines from different years (Fig. 6) reveals that the terminus was scoured out into multiple branches by meltwater. According to our statistics, GLJM Glacier's terminus length decreased ~415 m since 1988, which was a reduction of 13.8 m a⁻¹, twice the decrease in that of XDKMD Glacier.

Table 5. GLJM Glacier area change (AC) and area change rate (ACR) at different elevation intervals

Elevation (m)	05/09/1988–17/09/1998		17/09/1998–12/09/2008		12/09/2008–24/09/2018		05/09/1988–24/09/2018	
	AC (km² 10⁻²)	ACR (%)	AC (km² 10⁻²)	ACR (%)	AC (km² 10⁻²)	ACR (%)	AC (km² 10⁻²)	ACR (%)
5400–5450	−1.84	−4.3	−0.10	−0.2	−2.28	−5.6	−4.21	−9.9
5350–5400	−2.11	−5.7	−1.25	−3.6	−3.25	−9.6	−6.61	−17.8
5300–5350	−3.20	−9.9	−2.25	−7.8	−3.62	−13.5	−9.07	−28.2
5300–5250	−2.97	−13.2	−2.09	−10.6	−4.95	−28.2	−10.01	−44.3
<5250	−6.47	−31.9	−5.29	−38.3	−6.66	−78.0	−18.43	−90.8
Total	−16.59	−10.7	−10.98	−7.9	−20.76	−16.3	−48.33	−31.2
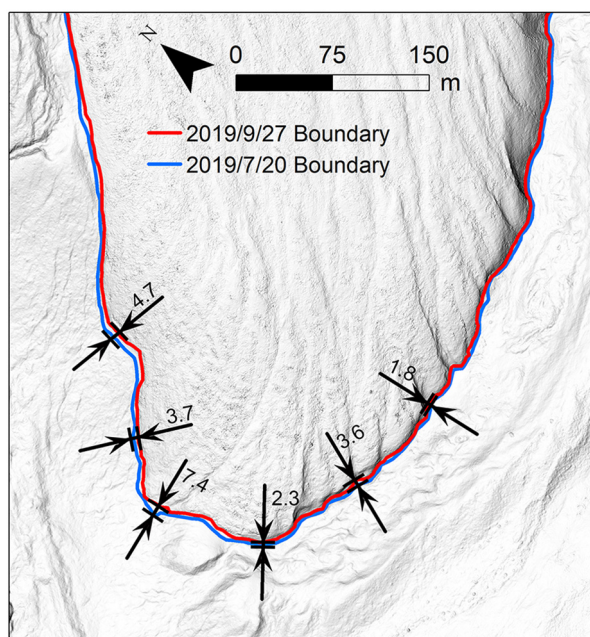
Fig. 8. Terminal length changes (meters) of XDKMD Glacier derived from two UAV surveys. The basemap is a hillshade generated from the DEM in 27/09/2019.

To assess glacier changes more accurately in each part, we divided the ablation zone into several elevation intervals based on the high-resolution DEM. As shown in Figure 7, the terminal part is always the region where ablation is strongest. For example, the region below 5350 m a.s.l. on XDKMD Glacier disappeared in 2008 (blue block in Fig. 7c), and after that, the region between 5400 and 5350 m (yellow block) was drastically reduced from 2008 to 2018, and its area shrunk ∼0.036 km², with an area change rate of 84.4% (Table 4). In addition, the terminal part of GLJM Glacier (blue block in Fig. 7d) decreased by ∼0.184 km² over the entire period, with an area change rate of 90.8%. While the region from 5400 to 5450 m decreased by only ∼0.042 km², with an area change rate of 9.9% (Table 5).

4.2 Glacier changes in recent years observed from UAV imagery

The high-resolution images obtained from the UAV are a significant improvement over the data obtained from satellite remote sensing. Based on the difference in the products generated from four aerial surveys, we calculated the terminal change and surface elevation change of XDKMD Glacier and GLJM Glacier in each corresponding period.

4.2.1 XDKMD glacier

The results show that XDKMD Glacier retreated with an average distance reduction of ∼3.9 m; decreased in terminal area of 2.3%, and area reduction of 0.0032 km² in the region below 5500 m a.s.l.

The western side of XDKMD Glacier exhibited stronger shrinkage than the eastern side of XDKMD Glacier during the ablation season. From Figure 8, the change in XDKMD Glacier from 20th July to 27th September can be seen in more detail.

Based on the high-resolution DEM, the surface elevation changes in the glacier terminus during the ablation season can be measured accurately. As shown in Figure 9, most regions in the ablation zone thinned ∼2–3 m. The marginal section of the glacier terminus had a relatively large elevation change, with a minimum ice loss of ∼3 m and a maximum ice loss of ∼8.5 m, which may be attributed to glacier retreat. Notably, several supraglacial drainage areas appeared on the terminus.

4.2.2 GLJM Glacier

Different from XDKMD Glacier, deep crevasses, which are clearly shown in Figure 10, formed on the surface of GLJM Glacier due to years of erosion by meltwater. These crevasses continue to widen and deepen as meltwater conduits have already formed. The area below 5400 m a.s.l. was reduced by 0.0529 km² during the last 2 years with an area change rate of 3.6% per year, and there is no doubt that the glacier terminus was the area where ablation was strongest, with an average retreat length of 49.7 m from 2017 to 2019.

As shown in Figure 11, the surface elevation of GLJM Glacier changed dramatically over the last 2 years, especially on the east side of the glacier margin (exact direction of sunlight in the morning) where the elevation changes even more than 16 m due to glacier shrinkage. Four main meltwater conduits on the top of the glacier separated the terminus into five branches, which will promote the formation of a fractured glacier and ice collapse and exacerbate glacier melting (Fig. 11f). Similar to the dirty surface (Fig. 11b), the meltwater remains that we captured near the conduits in July 2017 have a lower albedo than the surrounding area, which indicates intense glacier melting. Most regions of the terminus of GLJM Glacier show an ice loss of ∼5–12 m (Fig. 11a).

5. Discussion

5.1 Accuracy of the results

We determined the horizontal error of our results (length, area change) is about 3 pixels (0.27 m) by comparing stone positions in overlapping orthomosaics. Normally, the vertical error is larger than the horizontal error, especially in places with significant topographic changes. Thus, we selected several off-glacier zones to extract the elevation difference for quantifying the vertical accuracy of the results (elevation change). From the two histograms in Figure 12, we can see that the deviations in the off-glacier region in XDKMD Glacier and GLJM Glacier are controlled at ±0.5 m and ±1 m, respectively. Ideally, the elevation change in off-glacier area is zero. We interpreted such deviation as the following two causes: image quality (include overlap), error of reference products.
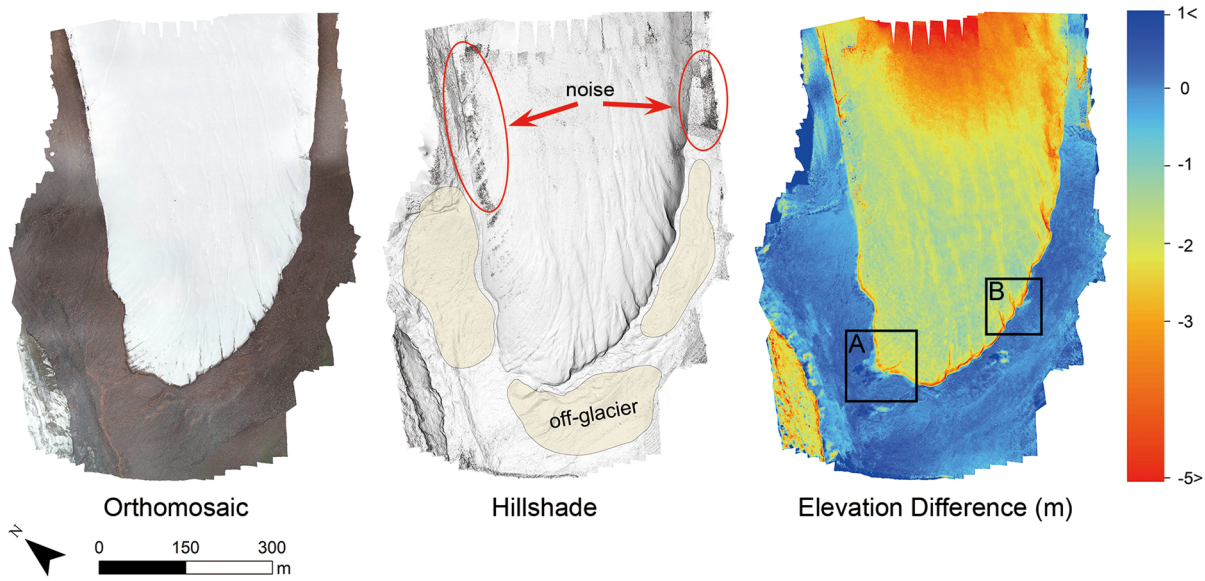
Fig. 9. Orthomosaic in 20/07/2019. Hillshade was generated from the DEM in 20/07/2019 (beige blocks are off-glacier area that outlined for accuracy validation). Elevation difference was detected from the DEMs in 27/09/2019 and 20/07/2019.
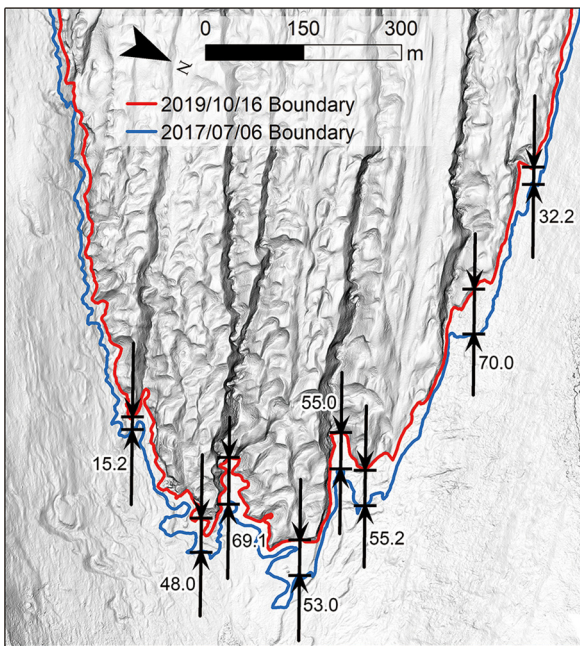

Fig. 10. Terminal length changes (meters) of GLJM Glacier derived from two UAV surveys. The basemap is a hillshade generated from the DEM in 16/10/2019.

The accuracy of our results is mainly influenced by image quality. Image acquirement in a high mountain glacier is challenging due to the hostile environment, such as unpredictable weather. We often encountered several weather events during one survey, and the images that we captured in different light conditions caused shadow stripes, as shown in the orthomosaic in Figure 11. Different light conditions may cause noise on point cloud, which can be seen clearly in the hillshade (Figs 9 and 11). The formation of such noise on point cloud is because the original images have different levels of shade which confused the matching algorithm. Additionally, the number of images that cover the edge of the survey zone is insufficient, and the point cloud that is generated from the images is relative sparse; thus, the edge of the products has low accuracy (Fig. 9).

The limitation of our research is lack of enough and well-distributed GCPs to improve and validate the accuracy of our final products. Thus, the absolute accuracy of the final products, which is poor, may influence other co-registered products. Additionally, the features we marked as MTPs are erratic boulders close to glacier. These erratic boulders around glacier may be influenced by glacier movement and topographic changes. And this may explain the reason that the vertical error of 2 years' change of GLJM glacier is slightly larger than that of seasonal change of XDKMD glacier. However, the settlement of GCPs in a high mountain glacier is a very difficult work. The sub-optimal method that quantifies the glacier change in a relative way has been proved feasible by previous research (Benoit and others, 2019).

5.2 Glacier surface characteristics

Comparing the ablation modes of the two glaciers, some commonalities exist. Although storage meltwater has not been detected on XDKMD Glacier, the beginning of a supra-glacial drainage area has developed, as shown in Figure 9. For GLJM Glacier, supra-glacial drainage areas have formed. Under the influence of these meltwater conduits, the terminus of the glacier was separated into multiple branches, which further facilitated ice collapse and fragmentation. In addition, these conduits are enlarged continuously and will lead to faster glacier recession. Despite this phenomenon, the formation of seracs in GLJM Glacier is not likely due to the fast recession speed.

Figure 13a shows the part with the longest retreating distance, which is also the direction that was once connected to the main glacier. As the terrain of this place is relatively lower, part of the glacial meltwater flows from here and joins the river. Several crevasses at the glacier terminus formed where the glacial meltwater flows occurred (Figs 13a, b). These crevasses have stronger ice loss than other nearby areas. With the continuous meltwater scouring along the existing trajectory, meltwater conduits may form on top of XDKMD Glacier, which would certainly accelerate glacier melting. More notably, the crevasses are dirtier than the surrounding area, which may explain why these crevasses melt faster than other areas.

There are many signs that indicate the rapid melting of GLJM Glacier, such as the undulating surface, storage water, dirty surface and ice collapse. The surface of the GLJM Glacier is undulating
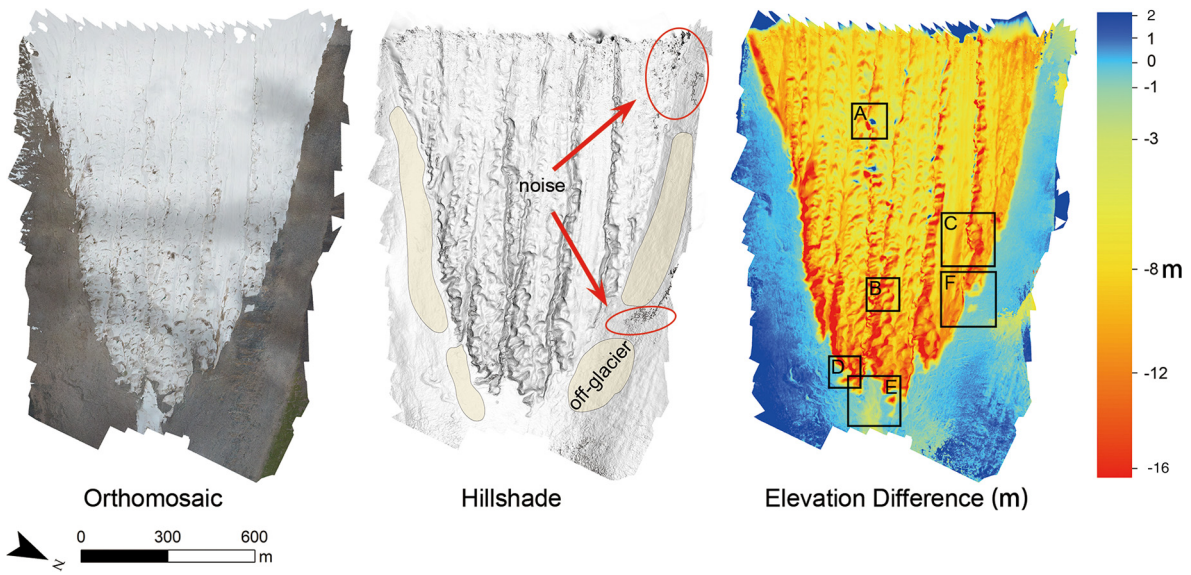
Fig. 11. Orthomosaic in 06/07/2017. Hillshade was generated from the DEM in 06/07/2017 (beige blocks are off-glacier area that outlined for accuracy validation). Elevation difference was detected from the DEMs in 06/07/2017 and 16/10/2019.
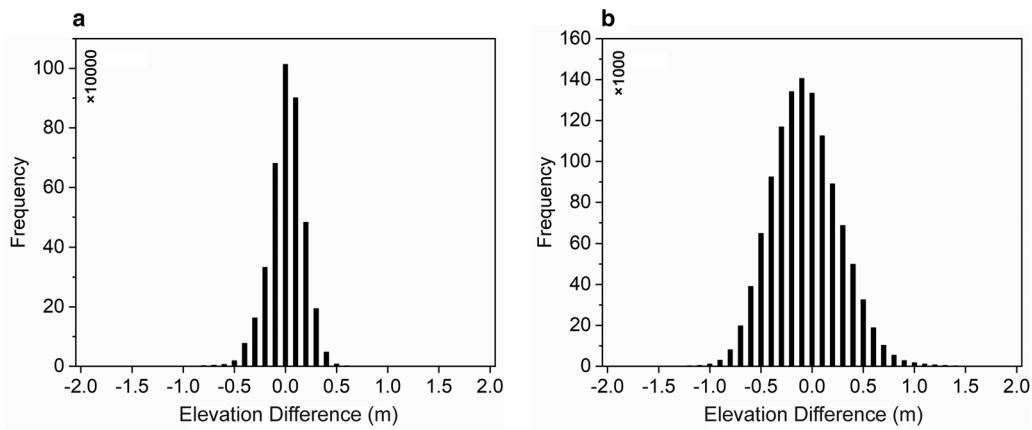

Fig. 12. Histograms show elevation change in the off-glacier areas of XDKMD Glacier (a) and GLJM Glacier (b). These areas have been outlined with beige blocks in Figures 9 and 11 hillshade, respectively.
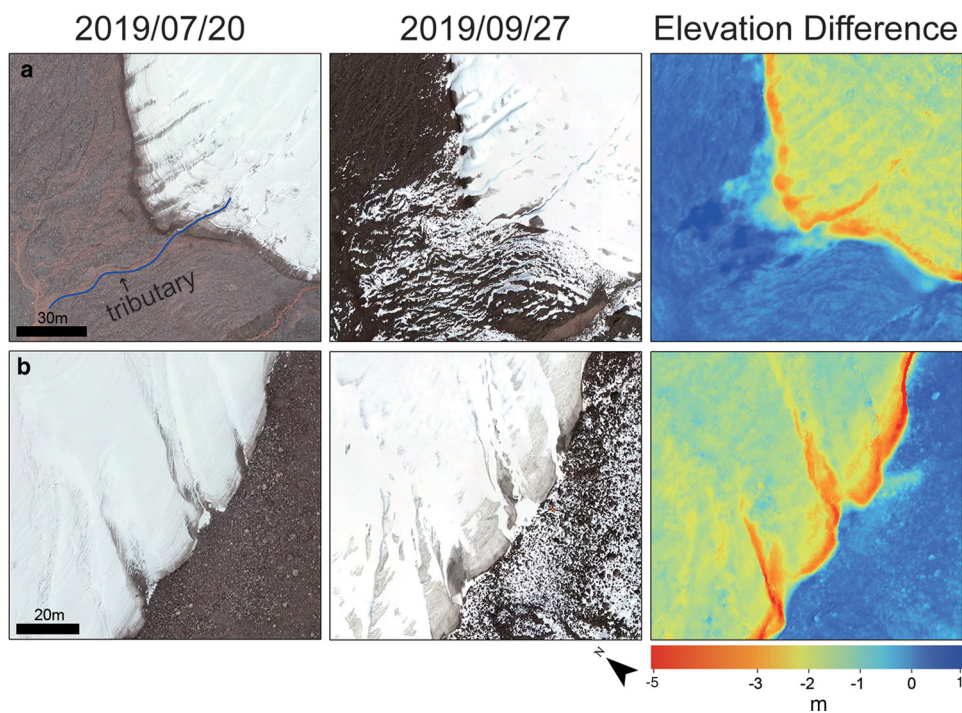

Fig. 13. Detailed changes in selected area in XDKMD Glacier (the location of these images is shown in Fig. 9). The left column shows the orthomosaic in 20/07/2019. The middle column shows the orthomosaic in 27/09/2019. The right column shows the elevation difference.

2017/07/06   2019/10/16   Elevation Difference
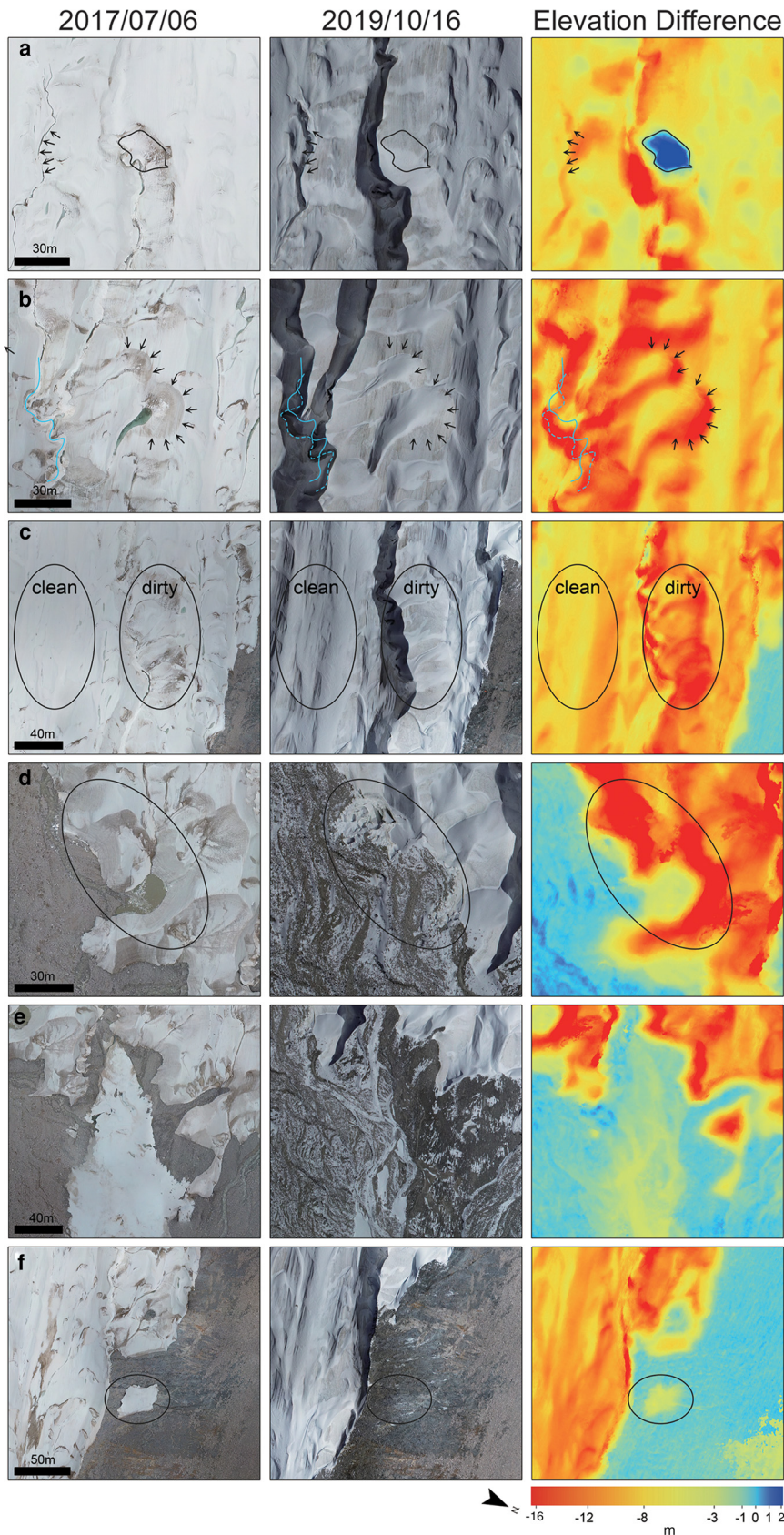
Fig. 14. Detailed change in selected area of GLJM Glacier (the location of these images is shown in Fig. 11). The left column shows the orthomosaic in 06/07/2017. The middle column shows the orthomosaic in 16/10/2019. The right column shows the elevation difference.

due to the heterogeneous surface ablation rate and erosion of meltwater. A positive balance is observed in several places on the terminal of GLJM Glacier, as shown in Figure 14a, the area encircled by a solid black line shows an increase in elevation of ~1–4 m. The arrow in Figure 14a points to a meltwater conduit. Apparently, the conduit has moved and deformed during the two UAV surveys. This movement is also displayed in Figure 14b.

Figure 14b shows an example of the existence of storage water on the surface of GLJM Glacier at the beginning of the ablation season. The water storage area has a lower albedo than the surrounding ice surface, resulting in faster ablation and unique erosional features.

We manually classified Figure 14c into two areas: the clean area and the relative dirty area. The dirty area, which is closer to the

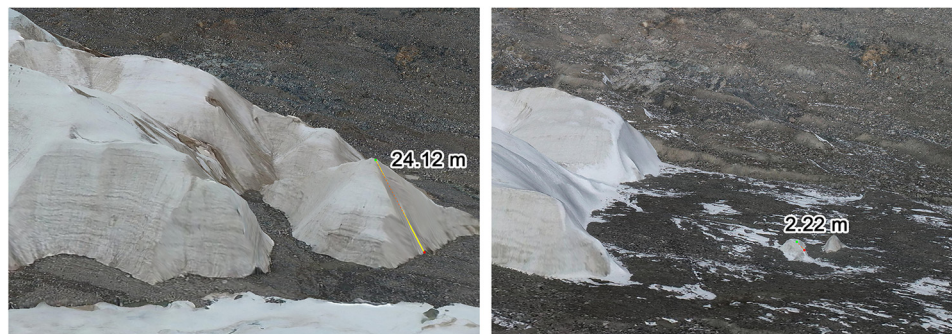**Fig. 15.** Ice collapse in the lateral branch in 2017 (left) and 2019 (right) in a 3D model view.

Fig. 16. Part of a fractured glacier in the terminus in 2017 (left) and 2019 (right) in a 3D model view.
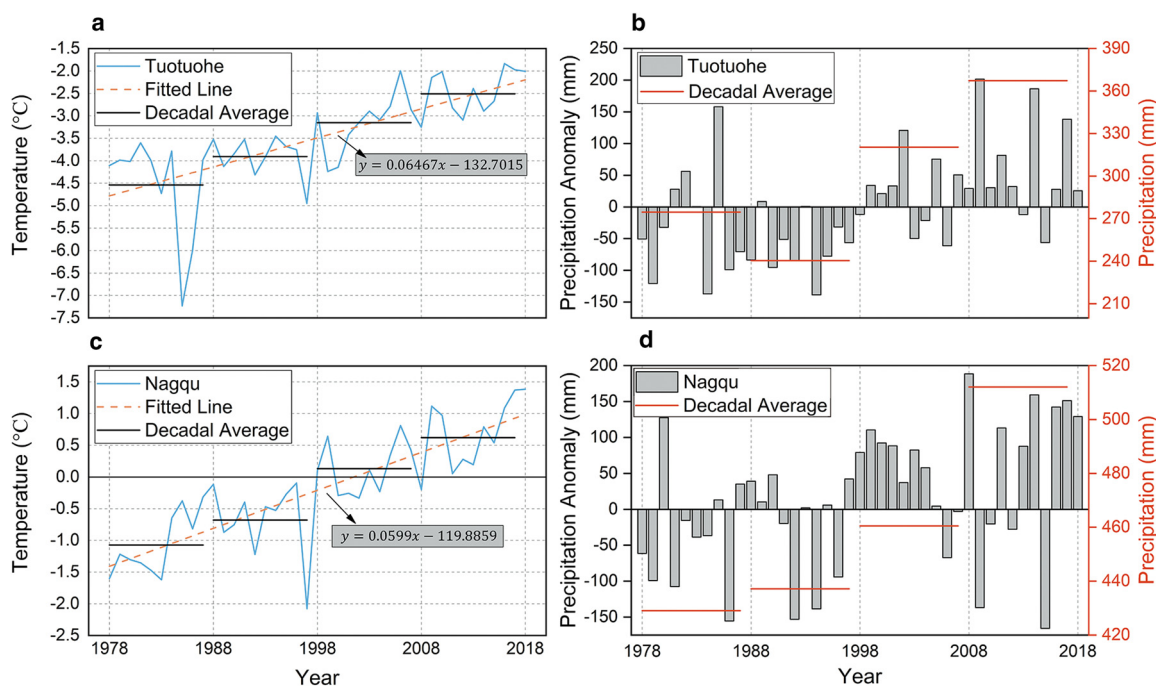

Fig. 17. Temperature and precipitation measured at Tuotuohe station and Nagqu station from 1978 to 2018.

meltwater conduit, has a larger mass loss than the clean area. We explained such phenomenon as the cause of enrichment of insoluble particles. Water from melting ice and snow flows down conduits, leaving insoluble particles to adhere to the glacier surface near these conduits. These particles reduce the albedo of glacier surface and further accelerate the melting process of glacier.

Figure 14d shows an ice collapse in the lateral branch of GLJM glacier, which may be caused by sub-glacial drainage or water erosion. This might indicate drastic ablation of GLJM glacier. Figure 15 provides another angle of this ice collapse in a 3D mode.

Figure 14e shows the river at the terminus of GLJM Glacier. The river water volume is very large in July due to the strongest glacier melting. Meanwhile, the thick river ice begins to melt (Fig. 2b). Until the end of September, when the glacier begins to enter the accumulation season, the river water volume decreases and the river ice melts completely. Therefore, there is a slight elevation change at the terminal river during each ablation season.

Figure 14f shows the fractured part of the glacier, which is a sign of the drastic ablation. The water erosion and attachment of the light absorbing impurities result in heterogeneous ablation

mode, which may lead to the formation of independent ice bodies. The fraction melts quickly which reveals that the formation of seracs in GLJM Glacier is impossible (e.g. Fig. 16).

5.3 Glacier response to climate change

Glacier change is one of the key indicators of climate change, and some works have shown that glaciers located at high altitudes, especially for those with small size, are more sensitive to climate change (e.g. Diolaiuti and others, 2012; D'Agata and others, 2014). Therefore, the rapid change in glaciers in our study area is likely indicative of local climatic fluctuations. To further understand why these glaciers changed so dramatically, we analyzed the data recorded by the automatic metrological station near the two glaciers.

A glacier's response to climate change has a time lag due to the downstream mass transport and deformation of the glacier (Pattyn, 2002), Wang and Zhang (1992) determined there was a time lag of about 12 years for glacier response to climate change in the Northern Hemisphere. Considering glaciers with small size are more sensitive to climate change, we assume there exist a decade lag in this paper and extend the beginning of the time series of the temperature and precipitation graphs to 1978. By an analysis of the temperature trends, we discovered that the annual mean temperature significantly changed in our study area since 1978 and both stations' records show very large rates of increase (Fig. 17). The annual rates of mean temperature increase at Tuotuohe station and Nagqu station are 0.65°C a^{-1} ($R^2 = 0.51$) and 0.60°C a^{-1} ($R^2 = 0.69$), much higher than the global warming magnitude 0.15–0.20°C a^{-1}. The annual precipitation shows a large fluctuation, which cannot be well fitted. Thus, we calculated the decadal average precipitation and temperature to make a better trend analysis, and a better comparison with the glacier changes in the corresponding period as well.

Compared with the first decade (1978–1988), the decadal average temperature in the second decade (1988–1998) rose by 0.64°C in Tuotuohe station and 0.39°C in Nagqu station, while the decadal average precipitation slightly increased (1.89% in Nagqu station) or even decreased (−12.45% in Tuotuohe station). This may explain why there was a reduced glacier area change rate in the following 10 years. Additionally, the sudden temperature dropped around 1997, which also reported by Ke and others (2017), may also contributed to this reduced change rate. The largest warming magnitude (0.76°C in Tuotuohe station; 0.81°C in Nagqu station) was between the second decade and the third decade (1998–2008). And at the meantime, decadal average precipitation had a comparable increase (33.29% in Tuotuohe station; 5.34% in Nagqu station), which should have slowed down glacier melting. However, the melting rate of these two glaciers did not decrease in the fourth decade (2008–2018), but reached its highest level in the past three decades with area change rate of 22.7% in XDKMD and 16.3% in GLJM glacier. Kang (1996) indicated that precipitation needs to increase by at least 40% to offset the effect of a one-degree rise in temperature on the glacier. Similarly, our analysis of glacier response to climate change might imply that slight increase in precipitation in our small study area made a limited contribution to glacier change, while rise in temperature has a greater impact on glacier.

6. Conclusion

In this study, we conducted four UAV surveys, for the first time, on two debris-free glaciers on the central TP. By co-registration of these UAV products, we quantified the termini, area and elevation change of the two glaciers in a short term, and further discussed surface characteristics based on the high-resolution products.

Additionally, we utilized eight Landsat scenes to measure the termini and area change of the two glaciers in the past 30 years. From the study, we draw the following conclusions.

During the last 30 years, the terminus of XDKMD Glacier retreated 176 m, with an area decrease of 0.17 km^2 (altitude below 5550 m a.s.l.), and the terminus retreat and area shrinkage of GLJM Glacier were 415 m and 0.18 km^2, respectively (altitude below 5450 m a.s.l.). The fastest decade of glacier melting occurred from 2008 to 2018. During this time, XDKMD Glacier retreated 9 m a^{-1} and had a terminal area shrinkage of 2.3% per year and GLJM Glacier retreated 16 m a^{-1} and had a terminal area shrinkage of 1.6% per year. During the ablation season, XDKMD Glacier retreated by 3.9 m; the terminal area shrank by 2.3%; and the surface elevation of most areas changed by 2–3 m. From 2017–2019, GLJM Glacier retreated by 24.9 m a^{-1}; the terminal area shrank by 3.6% per year; and the surface elevation of most areas changed by 8–12 m.

References

Andreassen LM, Paul F, Kääb A and Hausberg JE (2008) Landsat-derived glacier inventory for Jotunheimen, Norway, and deduced glacier changes since the 1930s. *The Cryosphere* **2**(2), 131–145. doi: 10.5194/tc-2-131-2008.

Benoit L and 9 others (2019) A high-resolution image time series of the Gorner Glacier – Swiss Alps – derived from repeated unmanned aerial vehicle surveys. *Earth System Science Data* **11**(2), 579–588. doi: 10.5194/essd-11-579-2019.

Bolch T and 7 others (2010) A glacier inventory for the western Nyainqentanglha Range and the Nam Co Basin, Tibet, and glacier changes 1976–2009. *The Cryosphere* **4**(3), 419–433. doi: 10.5194/tc-4-419-2010.

Brun F and 9 others (2016) Quantifying volume loss from ice cliffs on debris-covered glaciers using high-resolution terrestrial and aerial photogrammetry. *Journal of Glaciology* **62**(234), 684–695. doi: 10.1017/jog.2016.54.

Brun F and 9 others (2018) Ice cliff contribution to the tongue-wide ablation of Changri Nup Glacier, Nepal, central Himalaya. *The Cryosphere* **12**(11), 3439–3457. doi: 10.5194/tc-12-3439-2018.

Buri P, Pellicciotti F, Steiner JF, Miles ES and Immerzeel WW (2016) A grid-based model of backwasting of supraglacial ice cliffs on debris-covered glaciers. *Annals of Glaciology* **57**(71), 199–211. doi: 10.3189/2016AoG71A059.

Cao M, Li X, Chen X, Wang J and Che T (2006) *Remote Sensing of Cryosphere*. Beijing: Science Press.

Carrera-Hernández JJ, Levresse G and Lacan P (2020) Is UAV-SfM surveying ready to replace traditional surveying techniques? *International Journal of Remote Sensing* **41**(12), 4820–4837. doi: 10.1080/01431161.2020.1727049.

Che Y, Wang S, Yi S, Wei Y and Cai Y (2020) Summer mass balance and surface velocity derived by unmanned aerial vehicle on debris-covered region of Baishui river Glacier No. 1, Yulong snow mountain. *Remote Sensing* **12**(20), 3280. doi: 10.3390/rs12203280.

Colomina I and Molina P (2014) Unmanned aerial systems for photogrammetry and remote sensing: a review. *ISPRS Journal of Photogrammetry and Remote Sensing* **92**, 79–97. doi: 10.1016/j.isprsjprs.2014.02.013.

D'Agata C, Bocchiola D, Maragno D, Smiraglia C and Diolaiuti GA (2014) Glacier shrinkage driven by climate change during half a century (1954–2007) in the Ortles-Cevedale group (Stelvio National Park, Lombardy, Italian Alps). *Theoretical and Applied Climatology* **116**(1–2), 169–190. doi: 10.1007/s00704-013-0938-5.

Diolaiuti G, Bocchiola D, D'agata C and Smiraglia C (2012) Evidence of climate change impact upon glaciers' recession within the Italian Alps. *Theoretical and Applied Climatology* **109**(3–4), 429–445. doi: 10.1007/s00704-012-0589-y.

DJI (2017) Phantom 4 Pro/Pro+ User Manual v1.4. https://www.dji.com/uk/phantom-4-pro?site=brandsite&from=nav.

Fischer A, Seiser B, Stocker Waldhuber M, Mitterer C and Abermann J (2015) Tracing glacier changes in Austria from the Little Ice Age to the present using a lidar-based high-resolution glacier inventory in Austria. *The Cryosphere* **9**(2), 753–766. doi: 10.5194/tc-9-753-2015.

Furukawa Y and Ponce J (2010) Accurate, dense, and robust multiview stereopsis. *IEEE Transactions on Pattern Analysis and Machine Intelligence* **32**(8), 1362–1376. doi: 10.1109/TPAMI.2009.161.

Giordan D and 17 others (2020) The use of unmanned aerial vehicles (UAVs) for engineering geology applications. *Bulletin of Engineering Geology and the Environment* **79**, 3437–3481. doi: 10.1007/s10064-020-01766-2.

Guo W and 10 others (2015) The second Chinese glacier inventory: data, methods and results. *Journal of Glaciology* **61**(226), 357–372. doi: 10.3189/2015JoG14J209.

Guo W, Liu S, Xu J, Wei J and Ding L (2012) Monitoring recent surging of the Yulinchuan Glacier on north slopes of Muztag range by remote sensing. *Journal of Glaciology and Geocryology* **34**(04), 765–774.

Hall DK, Bayr KJ, Schöner W, Bindschadler RA and Chien JYL (2003) Consideration of the errors inherent in mapping historical glacier positions in Austria from the ground and space (1893–2001). *Remote Sensing of Environment* **86**(4), 566–577. doi: 10.1016/S0034-4257(03)00134-2.

Harwin S and Lucieer A (2012) Assessing the accuracy of georeferenced point clouds produced via multi-view stereopsis from unmanned aerial vehicle (UAV) imagery. *Remote Sensing* **4**(6), 1573–1599. doi: 10.3390/rs4061573.

Hodson A and 10 others (2007) A glacier respires: quantifying the distribution and respiration CO_2 flux of cryoconite across an entire Arctic supraglacial ecosystem. *Journal of Geophysical Research: Biogeosciences* **112**, G04S36. doi: 10.1029/2007JG000452.

Immerzeel WW and 6 others (2014) High-resolution monitoring of Himalayan glacier dynamics using unmanned aerial vehicles. *Remote Sensing of Environment* **150**, 93–103. doi: 10.1016/j.rse.2014.04.025.

Immerzeel WW, van Beek LPH and Bierkens MFP (2010) Climate change will affect the Asian Water Towers. *Science* **328**(5984), 1382–1385. doi: 10.1126/science.1183188.

Kääb A, Paul F, Maisch M, Hoelzle M and Haeberli W (2002) The new remote-sensing-derived Swiss glacier inventory: II. First results. *Annals of Glaciology* **34**, 362–366. doi: 10.3189/172756402781817473.

Kang E (1996) Characteristics of energy balance and computation on the mass balance change of the High-Asia cryosphere. *Journal of Glaciology and Geocryology.* **18**(S1), 12–22.

Kang S and 5 others (2010) Review of climate and cryospheric change in the Tibetan Plateau. *Environmental Research Letters* **5**(1), 015101. doi: 10.1088/1748-9326/5/1/015101.

Ke L, Ding X, Li W and Qiu B (2017) Remote sensing of glacier change in the central Qinghai-Tibet Plateau and the relationship with changing climate. *Remote Sensing* **9**(2), 114. doi: 10.3390/rs9020114.

Kraaijenbrink PDA and 5 others (2016*a*) Seasonal surface velocities of a Himalayan glacier derived by automated correlation of unmanned aerial vehicle imagery. *Annals of Glaciology* **57**(71), 103–113. doi: 10.3189/2016AoG71A072.

Kraaijenbrink PDA and 6 others (2018) Mapping surface temperatures on a debris-covered glacier with an unmanned aerial vehicle. *Frontiers in Earth Science* **6**, 64. doi: 10.3389/feart.2018.00064.

Kraaijenbrink PDA, Shea JM, Pellicciotti F, de Jong SM and Immerzeel WW (2016*b*) Object-based analysis of unmanned aerial vehicle imagery to map and characterise surface features on a debris-covered glacier. *Remote Sensing of Environment* **186**, 581–595. doi: 10.1016/j.rse.2016.09.013.

Küng O and 6 others (2012) The accuracy of automatic photogrammetric techniques on ultra-light UAV imagery. *ISPRS – International Archives of the Photogrammetry, Remote Sensing and Spatial Information Sciences* **3822**, 125–130. doi: 10.5194/isprsarchives-xxxviii-1-c22-125-2011.

Li Z, Sun W and Zeng Q (1998) Measurements of glacier variation in the Tibetan plateau using Landsat data. *Remote Sensing of Environment* **63**(3), 258–264. doi: 10.1016/S0034-4257(97)00140-5.

Liang L, Cuo L and Liu Q (2019) Mass balance variation and associative climate drivers for the Dongkemadi glacier in the central Tibetan Plateau. *Journal of Geophysical Research: Atmospheres* **124**(20), 10814–10825. doi: 10.1029/2019JD030615.

Lowe DG (1999) Object recognition from local scale-invariant features. *Proceedings of the Seventh IEEE International Conference on Computer Vision* **2**, 1150–1157. doi: 10.1109/ICCV.1999.790410.

Lowe DG (2004) Distinctive image features from scale-invariant keypoints. *International Journal of Computer Vision* **60**(2), 91–110. doi: 10.1023/B:VISI.0000029664.99615.94.

Mölg N and Bolch T (2017) Structure-from-Motion using historical aerial images to analyse changes in glacier surface elevation. *Remote Sensing* **9**(10), 1021. doi: 10.3390/rs9101021.

Pattyn F (2002) Transient glacier response with a higher-order numerical ice-flow model. *Journal of Glaciology* **48**(162), 467–477. doi: 10.3189/172756502781831278.

Paul F and 24 others (2015) The glaciers climate change initiative: methods for creating glacier area, elevation change and velocity products. *Remote Sensing of Environment* **162**, 408–426. doi: 10.1016/j.rse.2013.07.043.

Paul F, Kääb A, Maisch M, Kellenberger T and Haeberli W (2002) The new remote-sensing-derived Swiss glacier inventory: I. Methods. *Annals of Glaciology* **34**, 355–361. doi: 10.3189/172756402781817941.

Pix4D Professional photogrammetry and drone mapping software. https://www.pix4d.com/.

Pu J and 6 others (2008) Rapid decrease of mass balance observed in the Xiao (Lesser) Dongkemadi Glacier, in the central Tibetan Plateau. *Hydrological Processes* **22**(16), 2953–2958. doi: 10.1002/hyp.6865.

Qiao C (2010) Remote sensing monitoring of glacier changes in Dongkemadi region of Tanggula Mountain. *Journal of Anhui Agricultural Sciences* **38**(14), 7703–7705. doi: 10.13989/j.cnki.0.17-6611.2010.14.183.

Rossini M and 7 others (2018) Rapid melting dynamics of an alpine glacier with repeated UAV photogrammetry. *Geomorphology* **304**, 159–172. doi: 10.1016/j.geomorph.2017.12.039.

Turner D, Lucieer A and Watson C (2012) An automated technique for generating geo-rectified mosaics from ultra-high resolution unmanned aerial vehicle (UAV) imagery, based on structure from motion (SfM) point clouds. *Remote Sensing* **4**(5), 1392–1410. doi: 10.3390/rs4051392.

Vallet J, Panissod F, Strecha C and Tracol M (2011) Photogrammetric performance of an ultra-light weight swing-let 'UAV'. *ISPRS - International Archives of the Photogrammetry, Remote Sensing and Spatial Information Sciences* **3822**, 253–258. doi: 10.5194/isprsarchives-XXXVIII-1-C22-253-2011.

Vincent C and 10 others (2016) Reduced melt on debris-covered glaciers: investigations from Changri Nup Glacier, Nepal. *The Cryosphere* **10**(4), 1845–1858. doi: 10.5194/tc-10-1845-2016.

Wang N and Zhang X (1992) Mountain glacier fluctuations and climatic change during the last 100 years. *Journal of Glaciology and Greocryology* **14**(3), 242–250.

Whitehead K, Moorman BJ and Hugenholtz CH (2013) Brief communication: low-cost, on-demand aerial photogrammetry for glaciological measurement. *The Cryosphere* **7**(6), 1879–1884. doi: 10.5194/tc-7-1879-2013.

Wigmore O and Mark B (2017) Monitoring tropical debris-covered glacier dynamics from high-resolution unmanned aerial vehicle photogrammetry, Cordillera Blanca, Peru. *The Cryosphere* **11**(6), 2463–2480. doi: 10.5194/tc-11-2463-2017.

Yang W and 8 others (2020) Seasonal dynamics of a temperate Tibetan glacier revealed by high-resolution UAV photogrammetry and in situ measurements. *Remote Sensing* **12**(15), 2389. doi: 10.3390/rs12152389.

Yao T and 14 others (2012) Different glacier status with atmospheric circulations in Tibetan Plateau and surroundings. *Nature Climate Change* **2**(9), 663–667. doi: 10.1038/nclimate1580.

Ye Q, Kang S, Chen F and Wang J (2006) Monitoring glacier variations on Geladandong mountain, central Tibetan Plateau, from 1969 to 2002 using remote-sensing and GIS technologies. *Journal of Glaciology* **52**(179), 537–545. doi: 10.3189/172756506781828359.

Zhang J, He X, Ye B and Wu J (2013) Recent variation of mass balance of the Xiao Dongkemadi Glacier in the Tanggula range and its influencing factors. *Journal of Glaciology and Geocryology* **35**(02), 263–271. doi: 10.7522/j.issn.1000-0240.2013.0032.

Zhang Z, Jiang L, Liu L, Sun Y and Wang H (2018) Annual glacier-wide mass balance (2000-2016) of the interior Tibetan Plateau reconstructed from MODIS albedo products. *Remote Sensing* **10**(7), 1031. doi: 10.3390/rs10071031.

Zmarz A and 5 others (2018) Application of UAV BVLOS remote sensing data for multi-faceted analysis of Antarctic ecosystem. *Remote Sensing of Environment* **217**, 375–388. doi: 10.1016/j.rse.2018.08.031.